Supplementary Material (ESI) for Chemical Communications

Supplementary information for

A general route to synthesize supported isolated oxides and mixed-oxides nanoclusters at size below 5 nm

Magali Bonne, Djamila Sellam, Jean-Philippe Dacquin, Adam Fraser Lee, Karen Wilson, Luca Olivi, Andrea Cognigni, Patrice Marécot, Sébastien Royer* and Daniel Duprez

Synthesis procedure

SBA-15 type silicas: host supports were prepared according to Roggenbuck et al. procedure[S1] A mass of 12 g of triblock copolymer P123 is dissolved in 360 g of water and 43 g of HCl 32 wt.%. The solution is heated at 35 °C to allow the complete dissolution of the copolymer. 24 g of TEOS is slowly added under vigorous stirring given a gel composition of 1 TEOS: 0.018 P123 : 3.3 HCl : 187 H_2O (molar ratio). The solution is stirred at 35 °C during 24 h, transferred in a Teflon-line autoclave and heated at 50 (SBA15(6) sample), 100 (SBA15(8) sample) or 140 °C (SBA15(10) sample) during 24 h to obtain respectively a pore diameter of 6, 8 or 10 nm. The autoclave is cooled down to room temperature and the solid filtered, washed and dried at 80 °C overnight. Before use and characterization, supports are calcined under air at 550 °C during 3h (temperature increase ramp = 1 °C.min^{-1}).

Nanocomposite syntheses: masses of precursors ($La(NO_3)_3.6H_2O$, $Co(NO_3)_2.6H_2O$ for LaCo-based nanocomposite) were adjusted to give after impregnation and calcination, the desired loading 20 wt.% for $LaCoO_3$ and $CeNi_2O_y$ nanocomposites; 15 wt.% for Fe_2O_3 nanocomposite). Corresponding masses of nitrate precursors were first dissolved in 20 mL of distilled water, and glycine added as complexing agent (ratio $(NO_3)^-$/glycine = 1). After ageing, the glycine-nitrate precursor solution was mixed with 1.0 g of support freshly calcined, and water slowly evaporated under mixing. Temperature of the sample was then increased up to 280 °C for glycine auto-ignition. Before characterization, solids were calcined at 620 °C for 4 h.

Before use and characterization, all samples were analyzed by ICP-OES to verify bulk cation compositions. The measured compositions are summarized below.

Sample name	Expected composition	ICP measured composition
15Fe-SBA15(10)	15 wt.% Fe_2O_3 / SiO_2	16.1 wt.% Fe_2O_3 / SiO_2
20LaCo-SBA15(6)	20 wt.% $LaCoO_3$ / SiO_2	20.5 wt.% $La_{0.96}CoO_{2.94}$ / SiO_2
20LaCo-SBA15(10)	20 wt.% $LaCoO_3$ / SiO_2	20.9 wt.% $La_{0.95}CoO_{2.93}$ / SiO_2
20CeNi2-SBA15(8)	20 wt.% $Ce_{0.34}Ni_{0.66}O_{1.34}$ / SiO_2	20.3 wt.% $Ce_{0.32}Ni_{0.68}O_{1.32}$ / SiO_2

Characterization technique

TG-DSC experiment: measurements performed at each step of the synthesis on the 20LaCo-SBA15(10) sample: dried sample at 100 °C, after autocombustion step at 280 °C, after calcination at 620 °C. Signals were recorded between 50 °C and 800 °C under air flowing (total flow rate = 100 mL.min^{-1}, temperature increase rate = 5 °C.min^{-1}) on a TA SDT 2960 instrument.

Powder wide angle and small angle XRD: patterns were obtained on a Bruker AXS D5005 X-ray diffractometer, using a CuKα radiation (λ = 1.54184 Å) as X-ray source and equipped with a SolX detector. For small-angle analysis, signal was recorded for 2θ comprised between 0.75° and 2.5° with a step of 0.01° (step time of 10 s). For wide-angle analysis, signal was recorded for 2θ comprised between 15° and 50° with a step of 0.05° (step time of 2 s).

Specific surface area, pore size distribution and pore volume: Measurements were obtained from N_2 adsorption-desorption experiments. A known mass of sample was first outgassed under vacuum at 250 °C. Isotherms were obtained on a Micromeritics TRISTAR instrument. The specific surface area, S_{BET}, was calculated from the linear part of the BET plot. The mesopore size distribution was determined from the desorption branch using non local density functional theory (NLDFT) method. Calculation was performed using the Autosorb-1 1.55 software from Quantachrome. The kernel selected was N_2 on silica at -196 °C, assuming a cylindrical pore geometry and the metastability model based on the desorption branch. Mesopore volume was determined on the isotherms at $P/P_0 = 0.97$.

TEM coupled with Energy Dispersive X-ray spectroscopy (EDXS): pore structure as well as mixed-oxide particle composition and distribution within the silica grains were evaluated. Micrographs were collected on a JEOL 2100 instrument (operated at 200 kV with a LaB_6 source and equipped with a Gatan UltraScan camera). Cation homogeneity inside silica, and composition of the crystallized particles were evaluated by EDX spectroscopy. Analysis was repeated on several nanoparticles in order to reach a mean value of mixed-oxide composition. EDX spectroscopy was carried out with a JEOL 2100 microscope equipped with a Hypernine (Premium) detector (active area: 30 mm^2) using the software SM-JED 2300T for data acquisition and treatment. Analysis zone was defined for each particle observed and is generally ranging from 5 nm to 7 nm.

EXAFS and XANES: measurements on the Co K absorption edge were collected at the ELETTRA XAFS beamline operated at 2.4 GeV. Silicon (111) crystal monochromator was employed and the spectra were collected in transmission mode. The samples were prepared by grinding and mixing thoroughly the materials with boron nitride and formed into appropriate pellets. The $LaCoO_{2.5}$ sample was obtained by *in-situ* reduction (pure hydrogen) of $LaCoO_3$ for 1 h at 350 °C in the EXAFS cell. The data were processed by the Ifeffit software (Athena) and fitted by Excurve.

[S1] J. Roggenbuck, G. Koch, M. Tiemann, *Chem. Mater.*, **2006**, *18*, 4151-4156.

Supplementary characterization results

Table S1. Physical properties of the three used supports.

Solid	S_{BET}/ $m^2.g^{-1}$ [a]	D_p/ nm [a]	V_p/ $cm^3.g^{-1}$ [a]	V_{micro}/ $cm^3.g^{-1}$ [a]	d_{100}/ nm [b]
SBA15(6)-c550	590	5.7	0.58	0.11	7.3
SBA15(8)-c550	741	8.1	0.91	0.13	9.0
SBA15(10)-c550	532	9.5	1.20	0.04	8.7

[a] S_{BET} is the specific surface area obtained using the BET model, D_p is the mean pore diameter obtained using the NLDFT method on the desorption branch, V_p is the mesopore volume measured at P/P_0 = 0.97, V_{micro} is the micropore volume extrapolated from the t-plots; [b] d_{100} is the lattice spacing measured for the (100) reflection, obtained using low angle XRD.

Table S2. Cobalt oxidation state obtained by XANES for the three reference samples used for the linear XANES combination to evaluate mean oxidation state of cobalt in the nanocomposites.

Sample (XRD phase)	Co oxidation state		
	Co^{3+}	Co^{2+}	Co^0
$LaCoO_3$ (perovskite)[a]	100	0	0
$LaCoO_{2.5}$(brownmillerite)[b]	3	91	6
Co_3O_4 (spinel) [a]	67	33	0

[a], $LaCoO_3$ and Co_3O_4 purity was verified before use for EXAFS characterization. Only the desired phase was detected by XRD; [b], The $LaCoO_{2.5}$ sample was obtained by *in-situ* reduction of $LaCoO_3$ for 1 h at 350 °C in the EXAFS cell.

Table S3. EXAFS data parameters from Excurve fits for Co_3O_4, $La_2Co_2O_5$ and 20LaCo-SBA15 (6)

Sample	***Shell number***	***Shell***	***Parameter***		
			R	***N***	***A***
Co_3O_4	**1**	**Co-O**	**1.91**	**6**	**0.04**
	2	**Co-O**	**2.10**	**4**	**0.62**
	3	**Co-Co**	**2.84**	**4**	**0.01**
	4	**Co-Co**	**3.35**	**12**	**0.02**
$LaCoO_{2.5}$	**1**	**Co-O**	**1.96**	**5**	**0.03**
	2	**Co-Co**	**2.98**	**1**	**0.02**
	3	**Co-La**	**3.22**	**6**	**0.04**
	4	**Co-La**	**3.69**	**2**	**0.01**
	5	**Co-Co**	**3.99**	**4**	**0.03**
20LaCo-SBA15 (6)	**1**	**Co-O**	**1.90**	**4**	**0.02**
	2	**Co-Co**	**2.88**	**1**	**0.02**
	3	**Co-La**	**3.41**	**2**	**0.03**
	4	**Co-La**	**3.71**	**1**	**0.04**
	5	**Co-Co**	**3.97**	**2**	**0.04**

R = scattering distance / Å, N = coordination number, A = Debye-Waller factor / Å²

Table S4. Physical properties of the supported nanocrystalline $CeNi_2O_y$ doped oxide.

Solid	S_{BET}/ $m^2.g^{-1}$ [a]	Dp/ nm [a]	V_p/ $cm^3.g^{-1}$ [a]	V_{micro}/ $cm^3.g^{-1}$ [a]	ΔVp/ $\%.\%_{load}^{-1}$	d_{hkl}/ nm [b]	Crystal phase [c]
20CeNi2-SBA15(8)-c620	415.9 (522)	5.3 – 7.0	0.54	0.06	2.0	8.8	NiO

[a] S_{BET} is the specific surface area obtained using the BET model (*, in parenthesis: corrected surface area by removing the contribution of the weight gain consecutive to the introduction of the oxide phase), D_p is the mean pore diameter obtained using the NLDFT method on the desorption branch, V_p is the mesopore volume measured at P/P_0 = 0.97, V_{micro} is the micropore volume extrapolated from the t-plots; [b] d_{hkl} is the lattice spacing obtained using the (100) reflection in the 0.75-2.5°; [c] crystal phase identified by XRD.

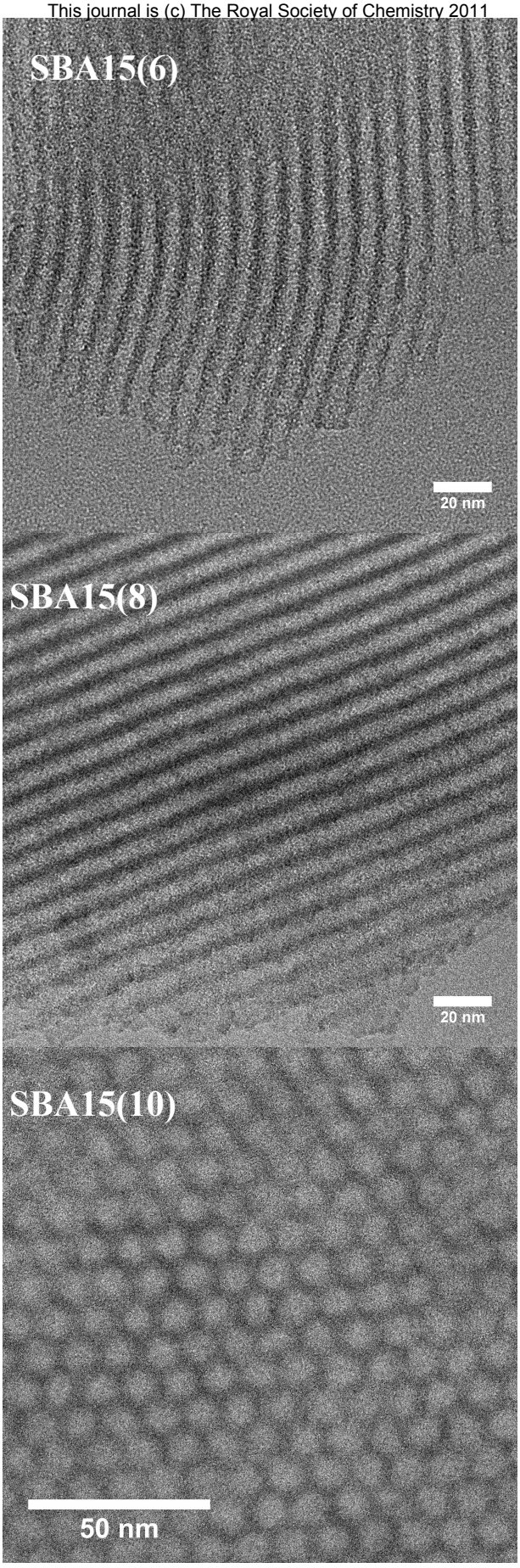

Figure S1. Typical TEM images obtained for the three SBA15-type silica supports used for the synthesis of the nanocomposites. Arrays (SBA15(6) and (SBA15(8) samples) and hexagonal symmetry of pore (SBA15(10) sample) are easily observed for the three samples.

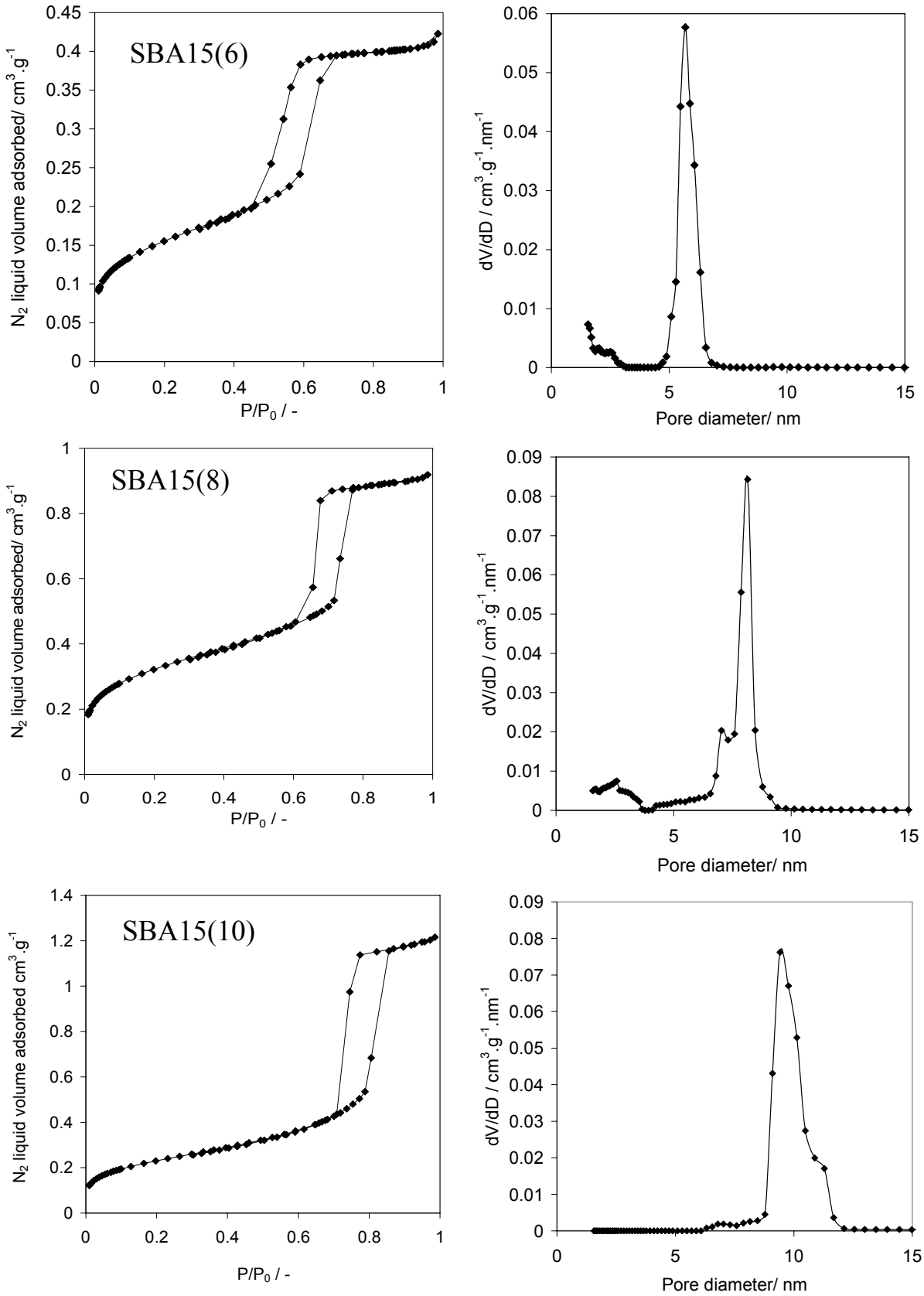

Figure S2. N_2- adsorption-desorption (left) and corresponding NLDFT pore size distribution obtained for the three SBA15-type silica supports used for the synthesis of the nanocomposites. Isotherms are of type IV according to the IUPAC classification, with brutal adsorption and desorption branches with a long adsorption plateau at high P/P_0. This kind of isotherm is characteristic of mesoporous solids. Parallel adsorption and desorption branches (type 1 hysteresis) clearly shows regular pores formation (cylindrical pores). The shift in P/P_0 of the adsorption and desorption branches between the three samples clearly shows the formation of solids having various pore sizes (see NLDFT pore size distributions obtained on the desorption branches, right).

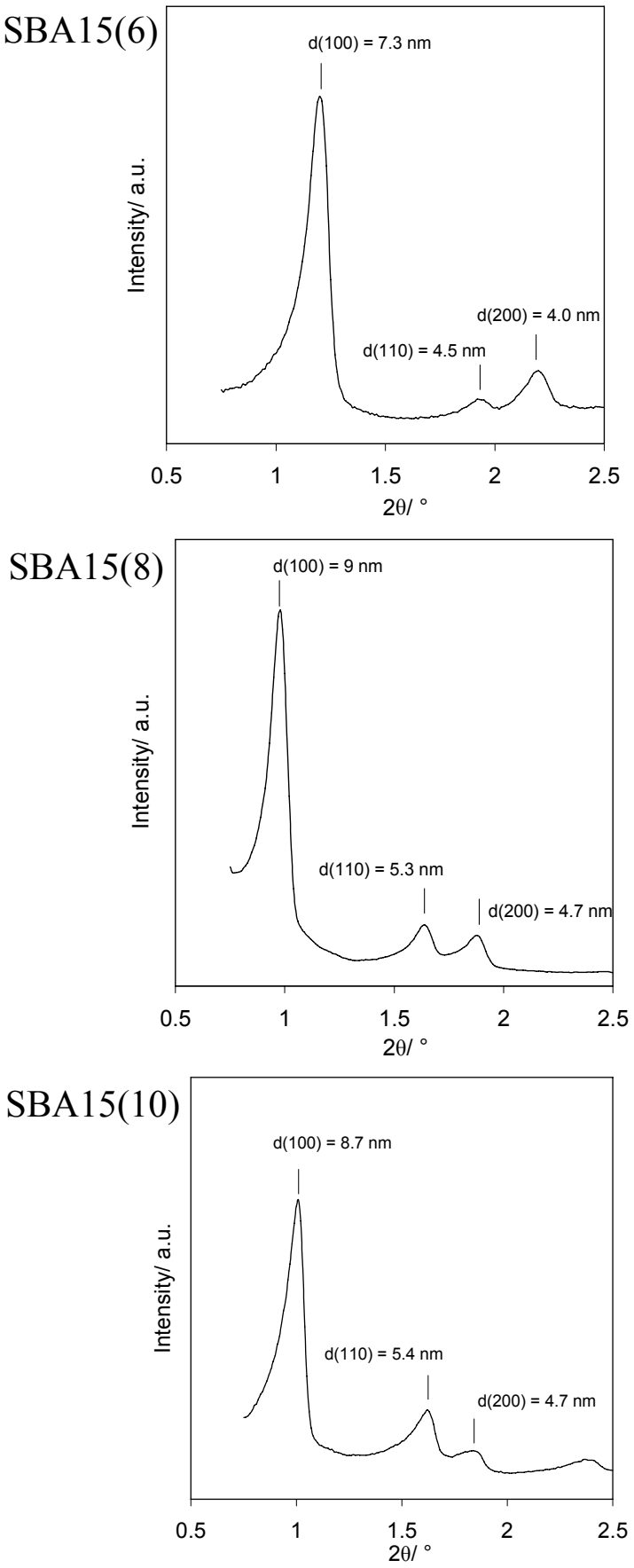

Figure S3. Small-angle X-ray diffraction patterns obtained for the three SBA15-type silica supports used for the synthesis of the nanocomposites. The three samples exhibit three distinct reflections characteristic of the (100), (110) and (200) lattice planes of the hexagonal pore structure symmetry. The easy detection of the three reflections is characteristic of a solid having a well-defined pore structure.

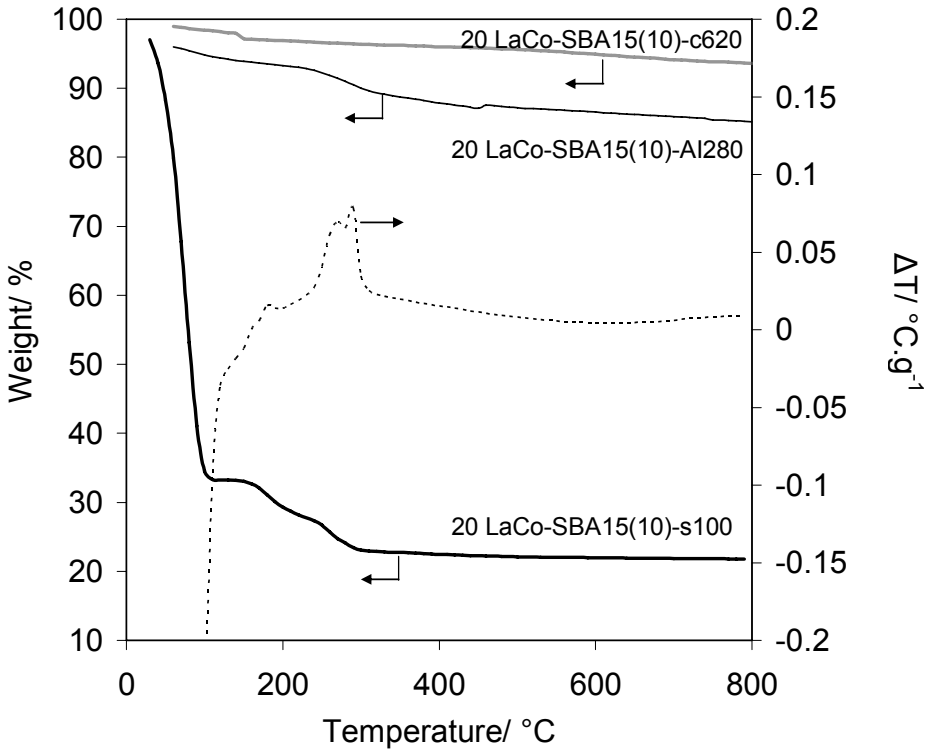

Figure S4. TG-DSC signal recorded on 20LaCo-SBA15(10) sample at each step of the synthesis: after drying at 100 °C (20LaCo-SBA15(10)-s100), after glycine autocombustion step at 280 °C (20LaCo-SBA15(10)-AI280), after final calcination step at 620 °C (20LaCo-SBA15(10)-c620. The TG curve of the sample dried at 100 °C exhibits a first weight loss below 100 °C attributed to water desorption. Then, two weight loss steps, accompanied by exothermal peaks (dotted line), are visible at higher temperatures (185 °C and 280 °C). These two exothermal steps are attributed to the autocombustion of glycine. The TG-DSC curves of the sample after autocombustion at 280 °C exhibit only one decomposition step at 280 °C, which can be attributed to the combustion of the residual unburned or partially decomposed glycine. Note that the fraction of residual unburned compound is limited (< 5%). After calcination (20LaCo-SBA15(10)-c620), no more exothermal phenomenon can be detected, indicating a complete autocombustion of the carbonaceous matter below this temperature.

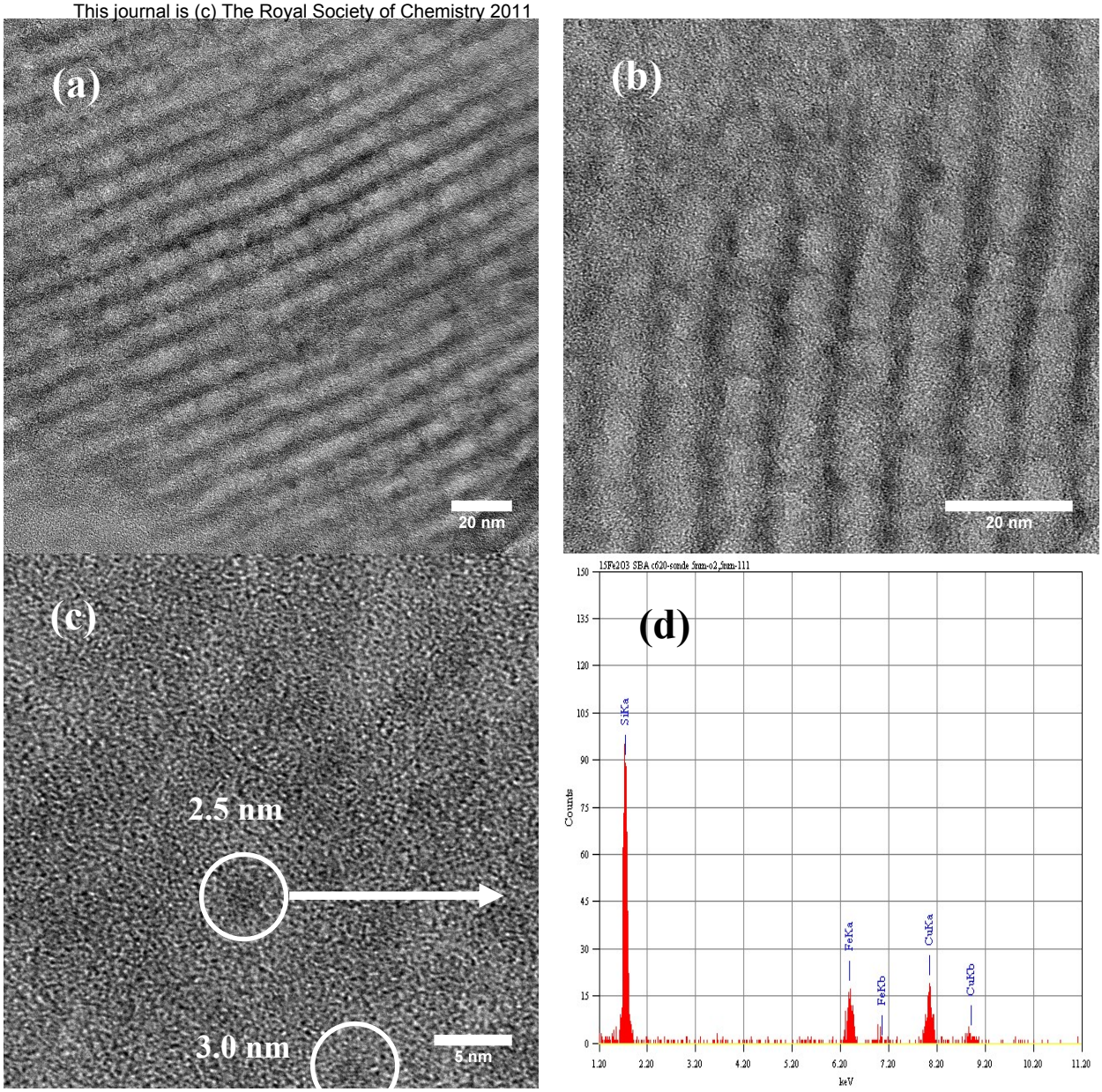

Figure S5. Typical TEM micrographs obtained for 15Fe-SBA15(10)-c620 sample. Low magnification images (a and b) show the presence of small darker spots. Focus on these darker spots (c) allows the detection of crystallized particles. Note that all darker spots do not exhibit crystal planes as in image (c) for which only the particle at 3.0 nm exhibits visible crystal plane. Nevertheless, EDXS analysis (d) of these darker spots always show the presence of iron.

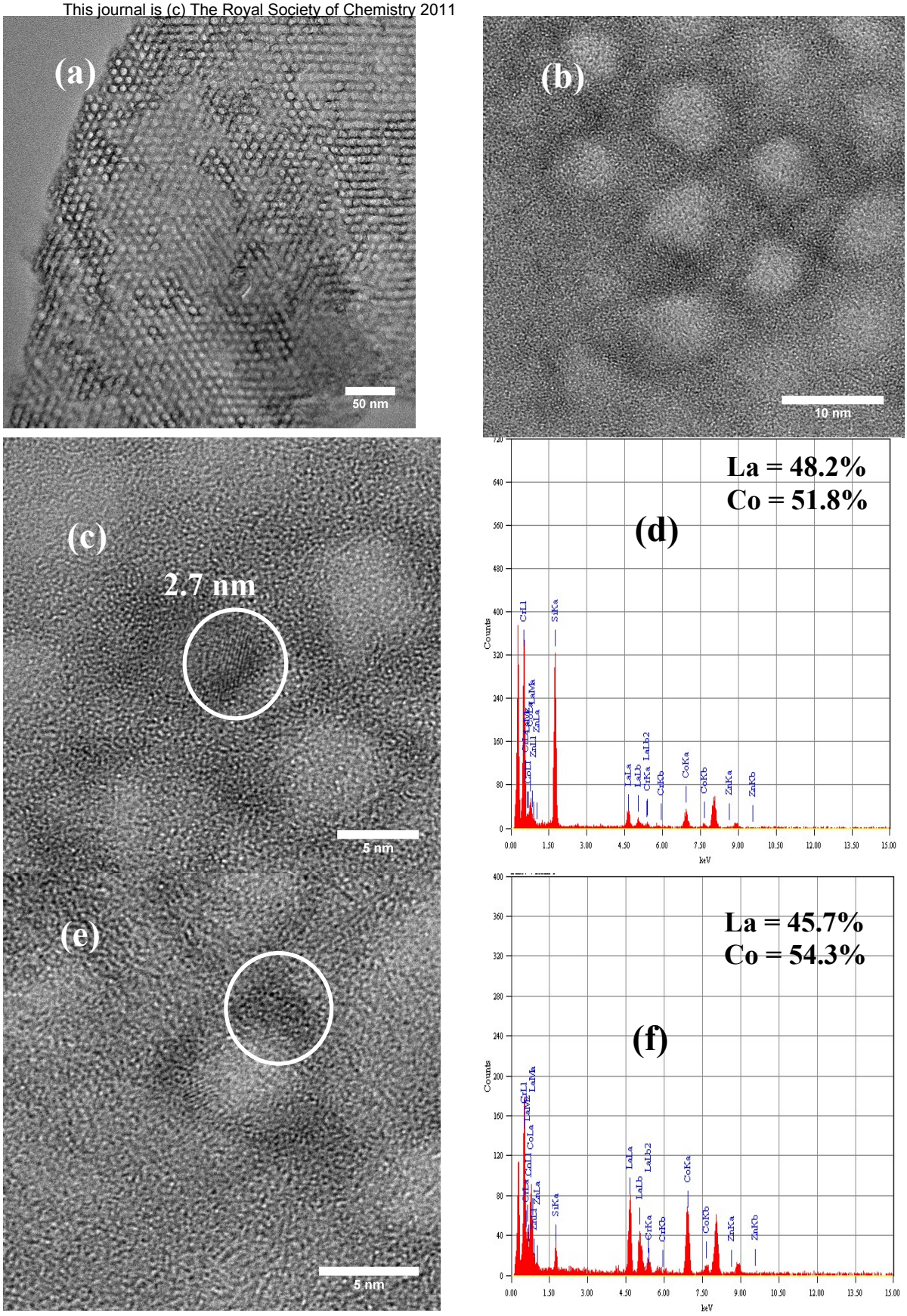

Figure S6. Typical TEM micrographs collected for 20LaCo-SBA15(10)-c620 sample. Low magnification images (a and b) show the presence of small darker zones, and it can be observed that these contrasts cover the pore circumference. No enrichment in darker matter on the periphery of the micrometric silica grains was observed during all the observation (a). Higher magnification on these darker zones allows the detection of crystallized particles (c and e). The size of the measured particles was always lower than 5 nm. EDXS measurements of the darker zones using a 5-7 nm analysis zone lead to La/Co atomic ratio always close to 1, suggesting a satisfying cation homogeneity in the particles close to the theoretical one.

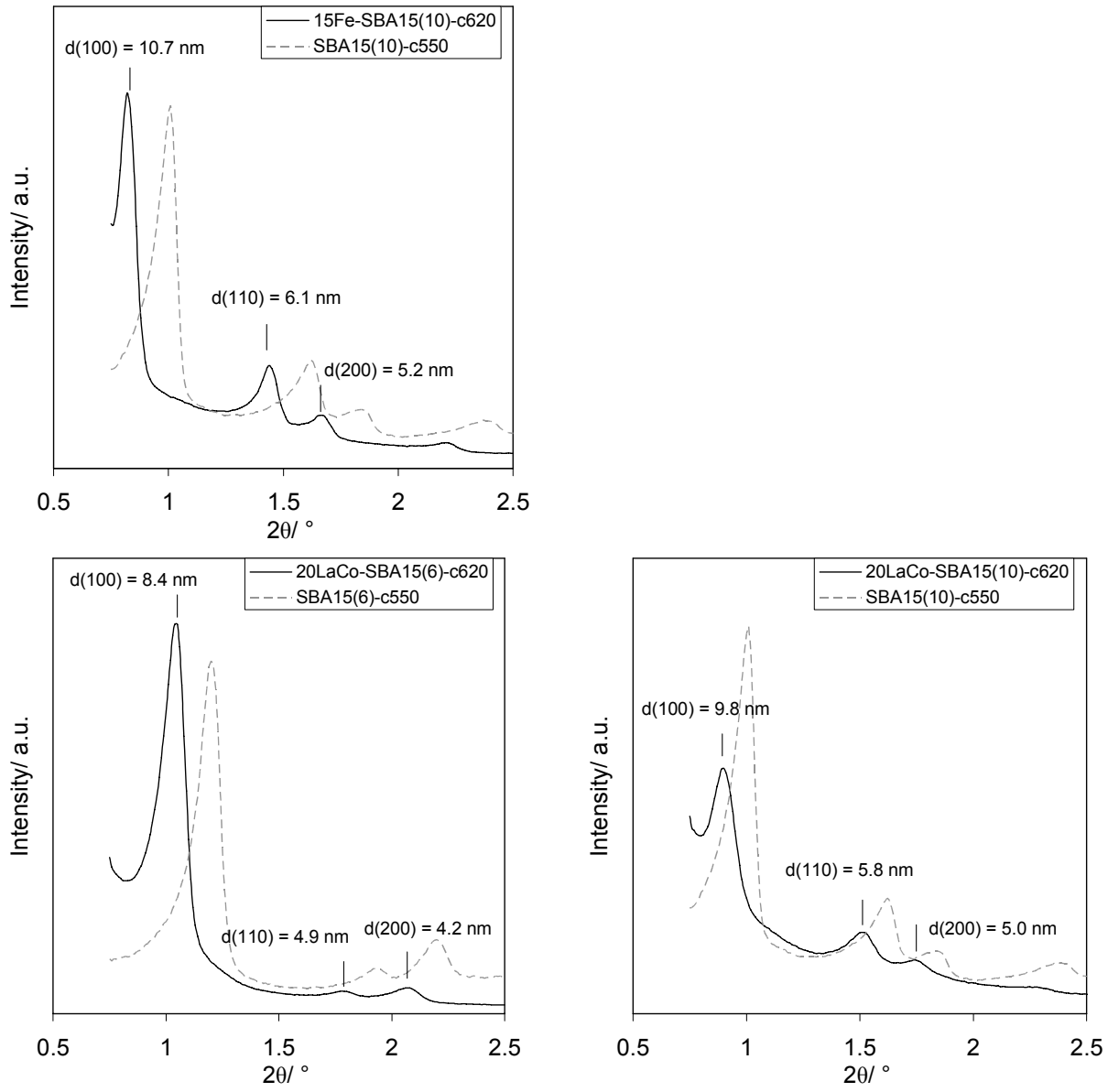

Figure S7. Small angle X-ray diffraction patterns obtained for Fe_2O_3 and $LaCoO_3$ based nanocomposites synthesized. Results obtained for bare supports are plotted in dotted line. All nanocomposite patterns exhibit three reflections, easily attributed to the (100), (110) and (200) planes of the hexagonal pore structure. Some fluctuation of the peak positions are noted in 2θ, suggesting some change in pore structure properties (fluctuation of the cell parameter, a_0). Nevertheless, the three peaks are still clearly visible (no important attenuation of their intensity), showing that the hexagonal pore structure remains unaltered in all case.

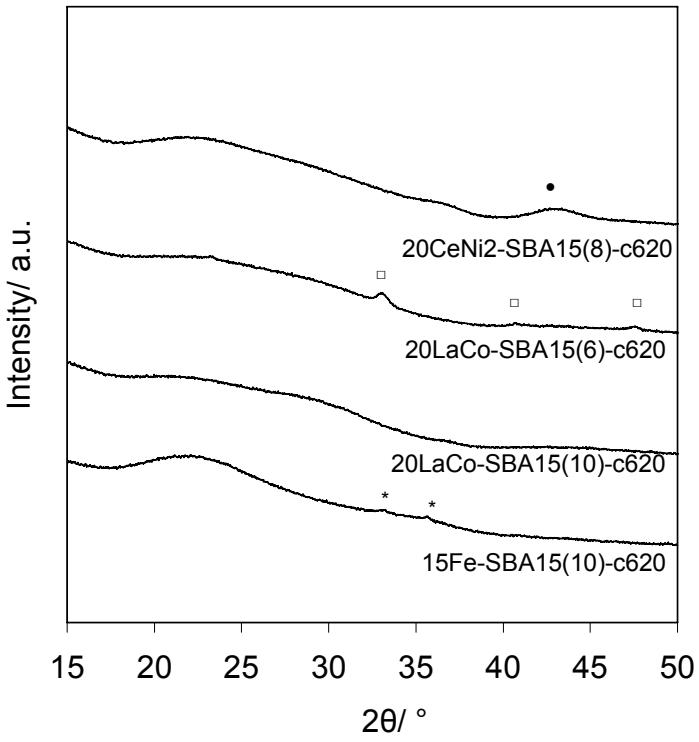

Figure S8. 15-50° X-ray diffraction patterns obtained for the four nanocomposites synthesized. •, NiO (JCPDS file n°047-1049); □, $LaCoO_3$ (JCPDS file n° 048-0123); *, Fe_2O_3 (JCPDS file n° 033-0664). Compared to bulk materials, analysis of the nanocomposites does not allow the detection of well-defined reflections. Indeed, a very broad reflection is observed at 42.9 °, and is identified as NiO. No reflection can be detected for 20LaCo-SBA15(10)-c620, while poorly defined and weak reflections at 33.2°, 40.9° and 47.5° are observed on 20LaCo-SBA15(6)-c620. These reflections are attributed to $LaCoO_3$ (JCPDS file n° 048-0123). Only very weak defined reflections of the hematite form of iron oxide can be detected at 33.2° and 35.7°.

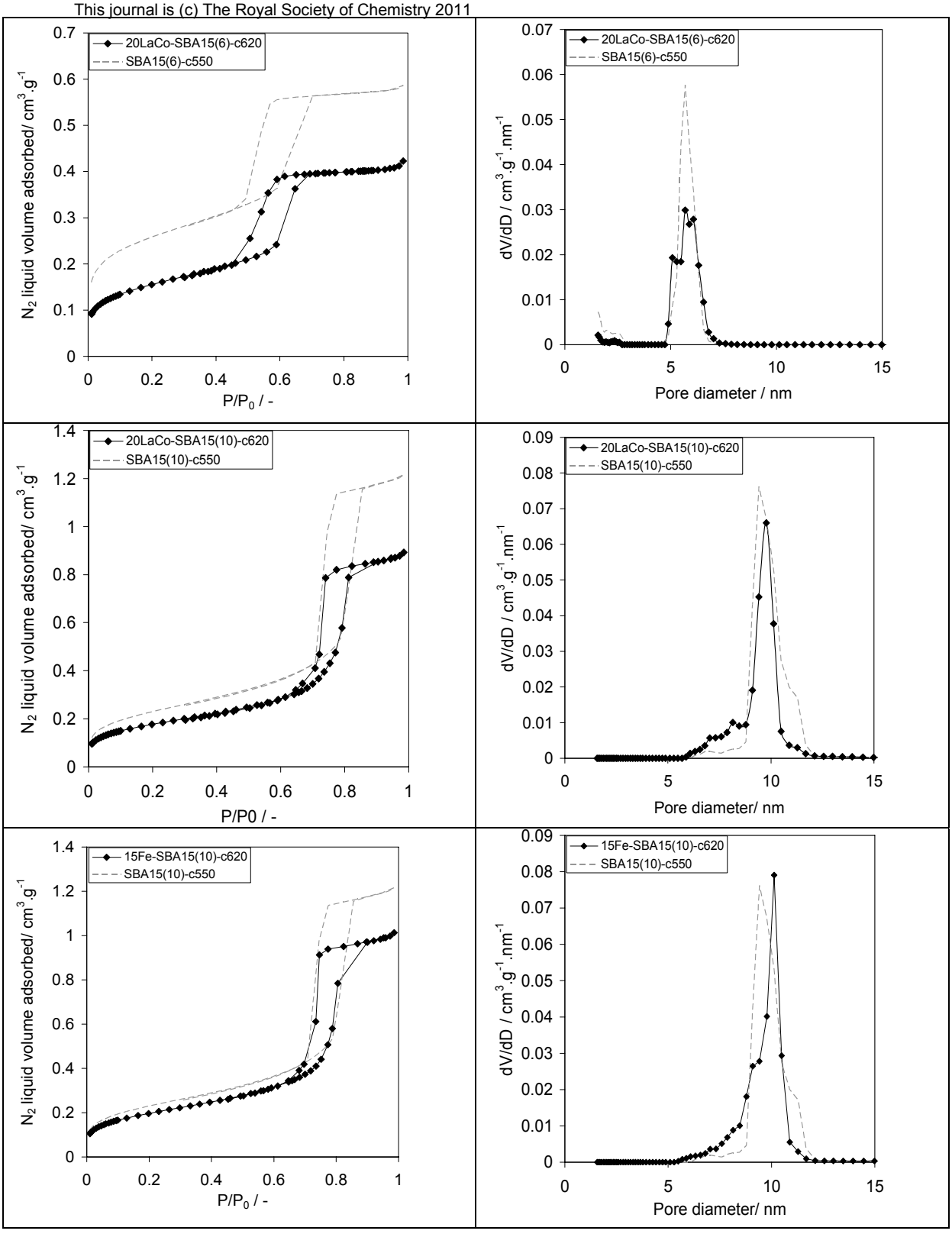

Figure S9. N_2 adsorption-desorption isotherms (left) and corresponding NLDFT pore size distribution (right) obtained for the four nanocomposites synthesized. Results obtained for the respective supports are plotted in dotted line. A pore volume decrease is noted for all the nanocomposites, with respect to the initial support. Isotherms remain of type IV, even if some changes in the hysteresis shape are observed after impregnation. This change in hysteresis shape from type 1 to type 2 is characteristic of a loss in cylindrical form of the pore, and formation of constrictions in the pores as expected in the case of nanoparticle deposition on the cylindrical pore surface of the initial SBA-15 supports.

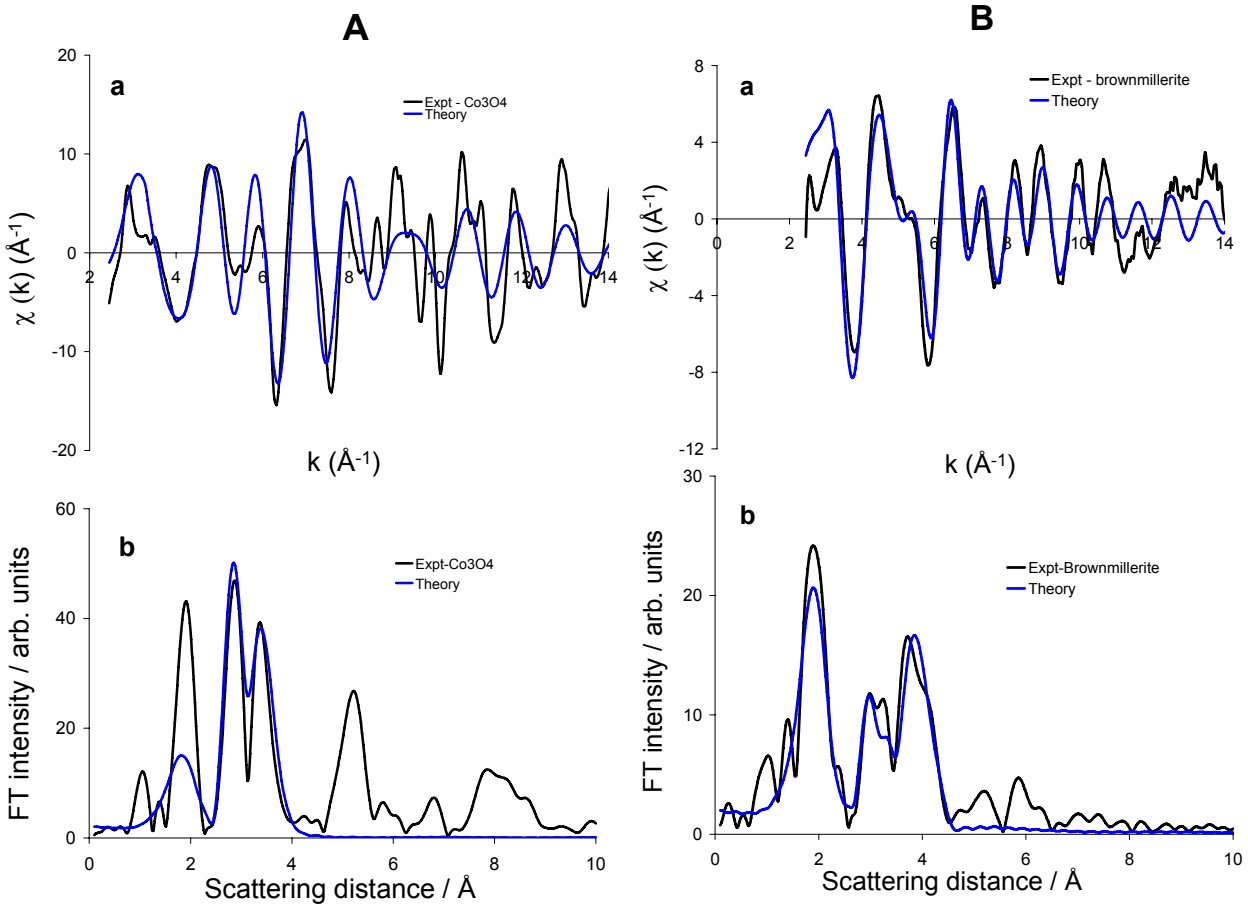

Figure S10. EXAFS measurements and calculations for Co_3O_4 (A) and $La_2Co_2O_5$ (B). Black curve: Raw experimental data after background subtraction. Blue curve : calculated using Excurve Software and the parameters shown in Table S4.

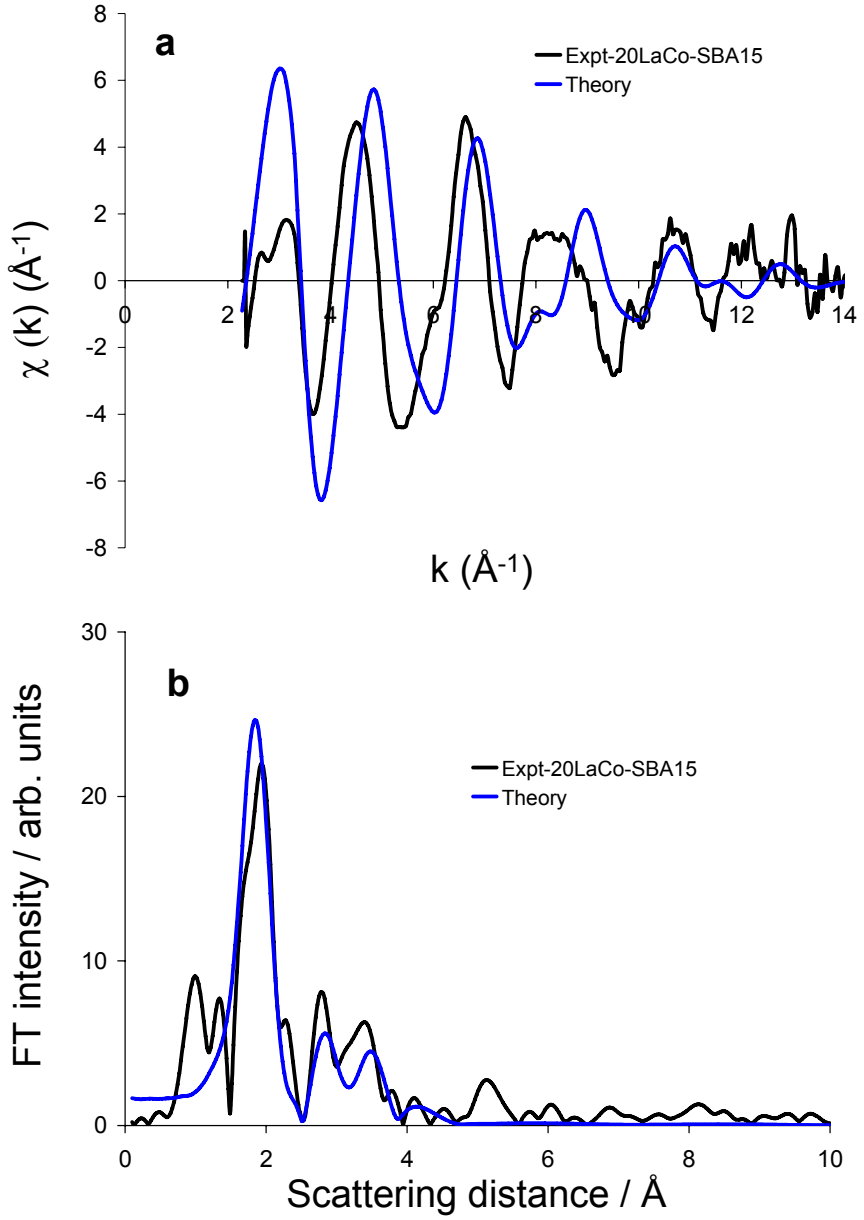

Figure S11. EXAFS measurements and calculations for 20LaCo-SBA15(6). Black curve: Raw experimental data after background substraction. Blue curve: calculated using Excurve Software and the parameters shown in Table S4.

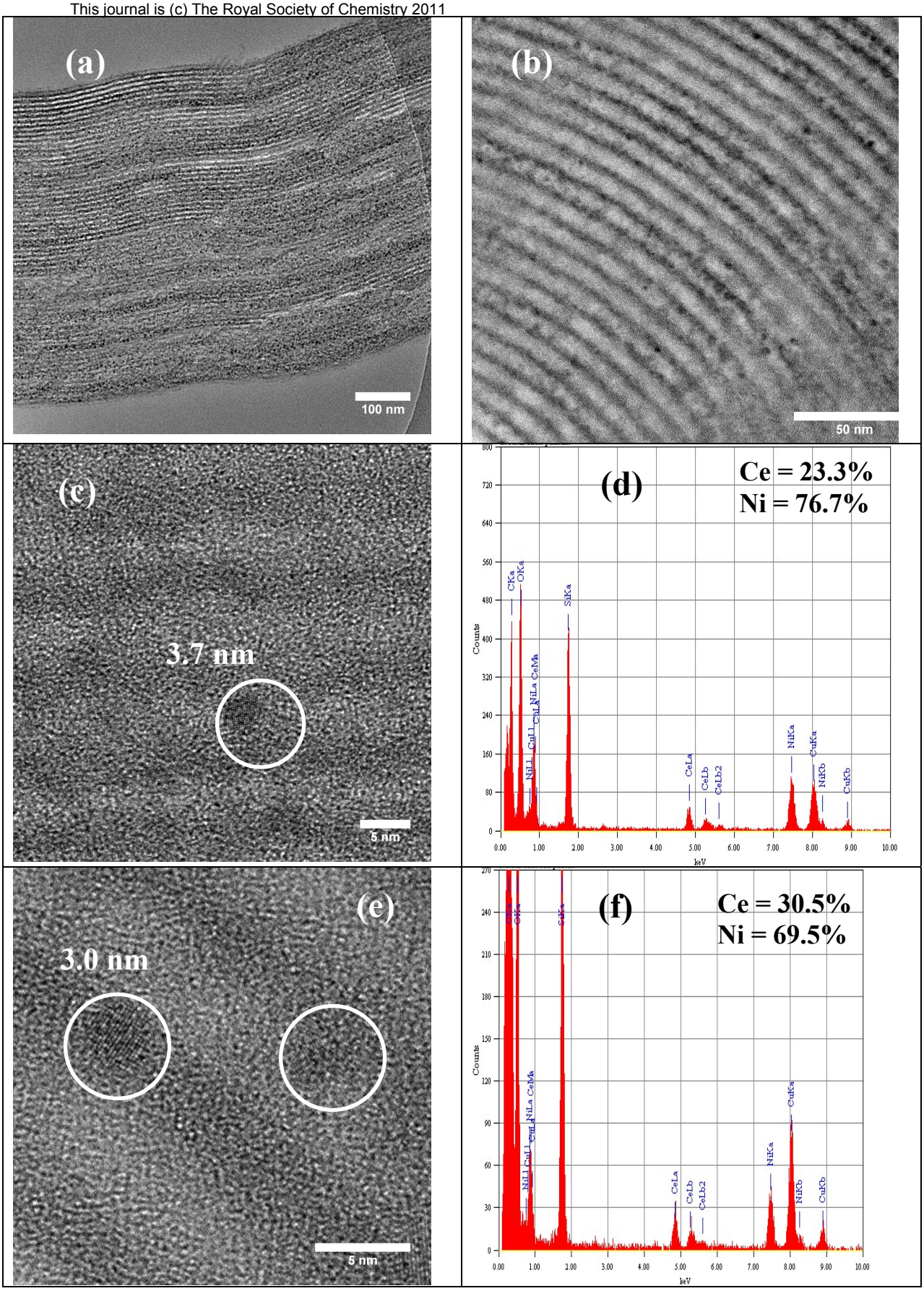

Figure S12. Supplementary TEM micrographs obtained for 20CeNi2-SBA15(8)-c620 sample. Low magnification images (a and b) show the presence of small darker spots within the silica porosity. No enrichment in darker matter on the periphery of the micrometric silica grains was observed during all measurements (a), whatever the sample analyzed. Focus on these darker spots reveals crystallized particles (c and e). The size of the measured particles was always lower than 5 nm, and generally below 4 nm. EDXS analysis of the crystallized particles using a 5-7 nm analysis zone lead to Ce/Ni atomic ratio always close to 0.5, suggesting a satisfying cation homogeneity in the particles close to the theoretical one.

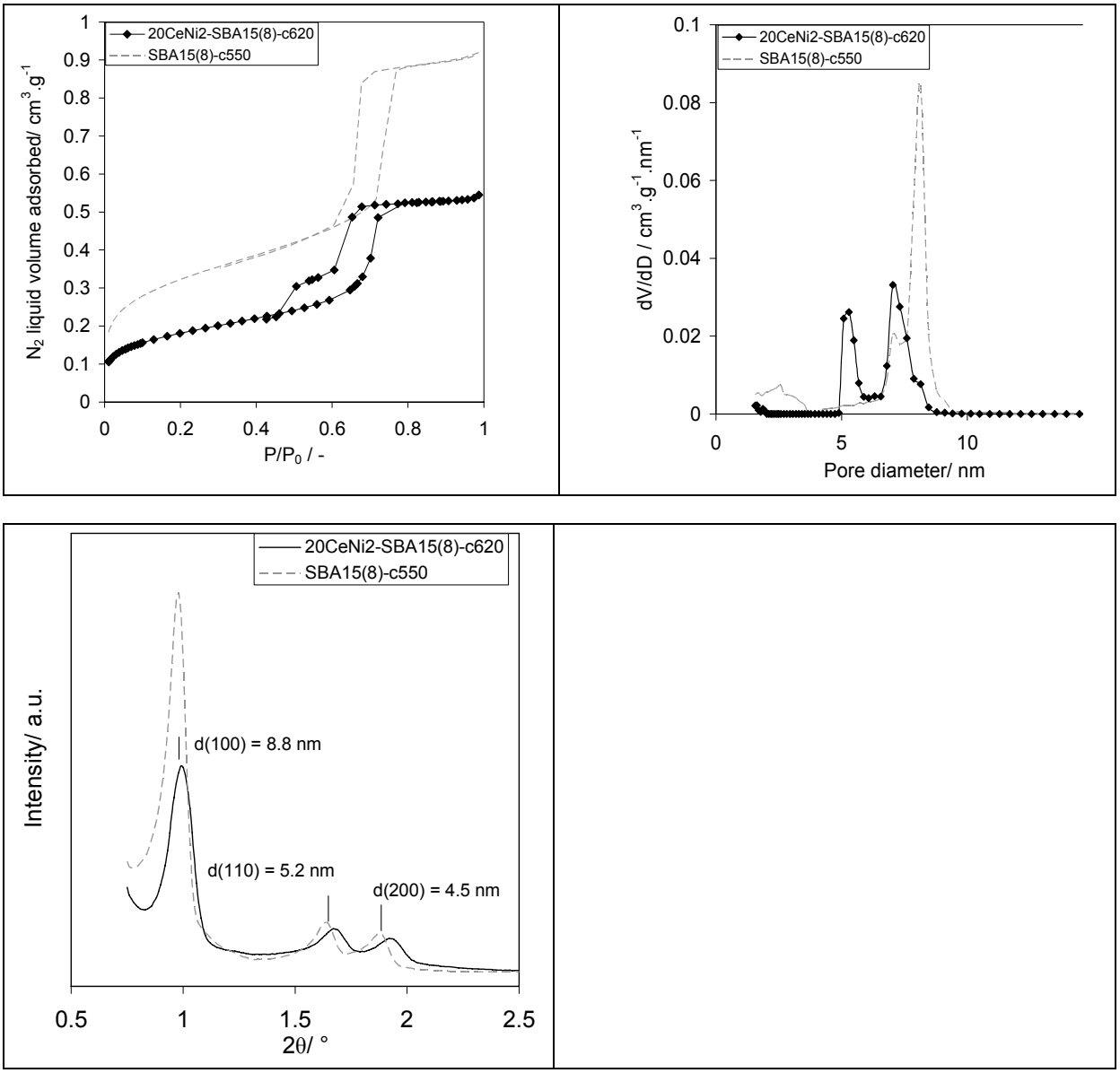

Figure S13. Textural properties of supported $CeNi_2O_y$ nanoparticles. **A)** N_2 adsorption-desorption isotherms ((left) and corresponding NLDFT pore size distribution (right). Results obtained for the respective support is plotted in dotted line. A pore volume decrease is noticed with respect to the initial support. Isotherms remain of type IV, even if some changes in the hysteresis shape are observed after impregnation. This change in hysteresis shape from type 1 to type 2 is characteristic of a loss in cylindrical form of the pore, and formation of constrictions in the pores as expected in the case of nanoparticle deposition on the cylindrical pore surface of the initial SBA-15 supports. Surprisingly, CeNi2-based nanocomposite presents a bimodal pore size distribution, with a pore size close to the parent support and a second pore size at 1.7 nm lower value.

B) Small angle X-ray diffraction patterns. Results obtained for the bare support is plotted in dotted line. The nanocomposite pattern exhibit three reflections, easily attributed to the (100), (110) and (200) planes of the hexagonal pore structure. Some fluctuation of the peak positions are noted in 2θ, suggesting some change in pore structure properties (fluctuation of the cell parameter, a_0). Nevertheless, the three peaks are still clearly visible (no important attenuation of their intensity), showing that the hexagonal pore structure remains unaltered.